Physics Faculty Publications and Presentations

Physics

2005

Making Sense of Nanocrystal Lattice Fringes

P. Fraundorf
University of Missouri - St Louis

Wentao Qin
Freescale Semiconductor, Inc.

Peter Moeck
Portland State University, pmoeck@pdx.edu

Eric Mandell
University of Missouri - St Louis

Citation Details

Making sense of nanocrystal lattice fringes

P. Fraundorf[a)]
*Department of Physics and Astronomy and Center for Molecular Electronics, U. Missouri-StL,
St. Louis, Missouri 63121*

Wentao Qin
Advanced Products R&D Laboratory, Freescale Semiconductor, Inc., Chandler, Arizona 85224

Peter Moeck
Department of Physics, Portland State University, P.O. Box 751, Portland, Oregon 97207-0751

Eric Mandell
*Department of Physics and Astronomy and Center for Molecular Electronics, U. Missouri-StL,
St. Louis, Missouri 63121*

The orientation dependence of thin-crystal lattice fringes can be gracefully quantified using fringe-visibility maps, a direct-space analog of Kikuchi maps [Nishikawa and Kikuchi, Nature (London) **121**, 1019 (1928)]. As in navigation of reciprocal space with the aid of Kikuchi lines, fringe-visibility maps facilitate acquisition of crystallographic information from lattice images. In particular, these maps can help researchers to determine the three-dimensional lattice of individual nanocrystals, to "fringe-fingerprint" collections of randomly oriented particles, and to measure local specimen thickness with only a modest tilt. Since the number of fringes in an image increases with maximum spatial-frequency squared, these strategies (with help from more precise goniometers) will be more useful as aberration correction moves resolutions into the subangstrom range. © *2005 American Institute of Physics*. [DOI: 10.1063/1.2135414]

I. INTRODUCTION

Nanocrystalline materials have attracted enormous interest due to their physical and chemical properties that differ from those of the bulk forms, thanks to proper engineering at the atomic level.[1] Phase diagrams and crystal morphologies are frequently dependent on the size of the crystals in the 1–10 nm size range.[2–4] In addition to this size dependence for the lowest-energy state of a structure, there is a strong tendency in the nanoparticle regime to metastability[5] and nonstoichiometry. Thus the need for characterization of individual nanocrystals will grow.

A simple approach in determining the lattice (not atomic) structure of nanocrystals, as though they were hand specimens with visible atom columns, was proposed in the late 1980s.[6] It relied on the three-dimensional (3D) reconstruction of lattice periodicities from images taken at different tilts. As in some diffraction-based techniques for obtaining 3D crystallographic information[7–21] as well as image-based techniques in stereomicroscopy[22] and electron tomography,[23–30] 3D information was inferred from two-dimensional (2D) projections. By way of followup, a recent direct determination of lattice parameters in three dimensions from images of a nanocrystal at two tilts[31] suggested that such lattice-only analysis strategies could be elegantly visualized using fringe-visibility maps that were quite sensitive to the effects of crystal thickness.

In this paper we investigate the visibility, versus orientation, of lattice planes which show up as fringes due to

scattering contrast effects when viewed nearly edge on. Such fringe contrast occurs, for example, in electron microscopes under both coherent (phase-contrast) and incoherent (*z*-contrast) imaging conditions. In this analysis, we concentrate specifically on phase-contrast mechanisms.

The concepts of visibility band and band maps are introduced. Bandwidths are to first order proportional to *d* spacing over thickness, rather than to wavelength over *d* spacing as in the case of Kikuchi,[32] bend contour,[33,34] electron-channeling pattern,[35] and backscatter-electron-diffraction[36] bands in thicker specimens. Applications examples include (1) image-based protocols for the acquisition of three linearly independent lattice-plane normals from a single randomly oriented nanoparticle, each parallel to an operating reflection *g* vector, (2) predicting fringe and cross-fringe abundances in a collection of randomly oriented particles for comparison to experimental data, and (3) measuring local specimen thickness by observing variations in fringe visibility during tilt.

II. METHODS

The transmission electron microscope (TEM) used is a Philips EM430ST with a point resolution near 0.2 nm. Although lattice-fringe information is often available in electron phase-constrast images out to the "information limit," for simplicity we only consider fringes out to the continuous transfer or "point resolution at Scherzer defocus" *for a given image* since the absence of smaller fringes may be due to zeros in contrast transfer. Hence talk here of "point-resolution" limits is a shorthand for saying that deductions here consider only fringes whose presence in the subspeci-

[a)]Electronic mail: pfraundorf@umsl.edu

98, 114308-1

men electron wave field is reliably transferred to the recorded image. Data from two samples were used for experimental measurements of the probability of visualizing ⟨001⟩ zone fringes. The first contained Au/Pd nanocrystals, which were sputtered onto a thin carbon film with a Hummer IV sputter coater. The second sample was a nanocrystalline tungsten carbide thin film, deposited by plasma-enhanced chemical-vapor deposition (PECVD).

III. OBSERVATIONS

A. Fringe-visibility bands

Our goal is to explore the direct-space geometry of fringe visibility. Connections between electron-diffraction theory and high-resolution electron microscope imaging (cf. Reimer[34] and Graef[37]) provide guidance, as follows. On tilting away from the edge-on view of a lattice plane, one encounters a range of incident electron angles (e.g., relative to lattice-plane parallel) within which the lattice plane's reciprocal lattice spots continue to intersect the Ewald sphere.[38] Hence lattice fringes associated with those planes remain visible. As shown in Appendix A, the upper bound of this range (with the largest term first in our "thin specimen" limit) is

$$\alpha_{max} = \sin^{-1}\left\{d\frac{\Gamma}{t} + \frac{\lambda}{2d}\left[1 - \left(d\frac{\Gamma}{t}\right)^2\right]\right\}. \quad (1)$$

Here d is the spacing of the lattice planes, t is the crystal thickness, λ is the wavelength of the electrons, and Γ is a "visibility factor" on the order of 1 that empirically accounts for the signal-to-noise ratio in the method used to detect fringes. The effective radius of the reciprocal lattice spot in this model (or excitation error s at which the fringe fades to background) is Γ/t. For example, when $\Gamma=1$ this is the first zero in $\sin[\pi g t]/(\pi g t)$: the signal-processing Fourier transform of a unit-area boxcar function, that convolved with the transform of an infinite lattice, yields the transform of a finite lattice of thickness t. The above calculation of α_{max} is based on the kinematic model, which should work well between zones (i.e., under two-beam conditions) since scattering is kinematic when the diffracted beam is about to extinguish.

For much of this paper, we assume that lattice fringes are visible when the electron beam lies parallel to a set of lattice planes. As shown in Appendix B, for thick crystals under parallel illumination this may not be the case of α less than some α_{min}. Our assumption that $\alpha_{min}=0$ is typically valid for crystals in the 10 nm and smaller size ranges.

Two symmetries shall be taken into account when considering lattice-fringe visibility versus the incidence direction. The symmetries are an azimuthal symmetry of the electron beam about the normal of the lattice planes and a mirror symmetry about the lattice planes. This consideration leads to the concept of fringe-visibility band.

Such a visibility band is a schematic representation of an ensemble of electron-beam incident directions. These directions are so defined that when the electron beam is along any of them, the lattice fringes are visible. As shown in Fig. 1, every point on the surface of the sphere simply and elegantly represents a radially inward direction. The ensemble of orientations from which a set of lattice planes is visible forms a
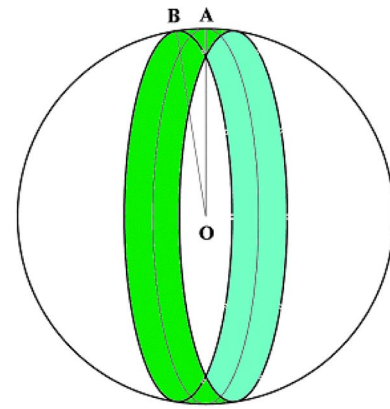

FIG. 1. (Color online) The visibility band (shaded) of a set of spherical crystal lattice planes whose trace follows the great circle through *A*. Lattice fringes disappear as the electron beam is tilted from any point along the trace in a direction perpendicular to the trace circle by an angle greater than the angle $AOB = \alpha_{max}$, the visibility-band half-width.

visibility band on the surface of the sphere. The projection of a lattice plane itself is a great circle, about which the visibility band is symmetric.

For thin specimens and the small λ/d of typical electron microscopes, Eq. (1) simplifies to $\alpha_{max} \cong \sin^{-1}(\Gamma d/t) \cong \Gamma d/t \propto d$. Therefore visibility bands are different from Kikuchi bands in that the bandwidth is proportional (rather than inversely proportional) to lattice spacing. Thus we think of visibility bands as tools of "direct-space crystallography."

B. Fringe-visibility maps

The ensemble of all the visibility bands of a spherical crystal forms a fringe-visibility map. The band map not only reveals the crystal lattice symmetry and spacing, but also is TEM specific, i.e., only resolvable lattice-plane sets have their bands on the map. Figure 2 shows such a map. Some examples to appreciate the crystallographic information in fringe-visibility maps are given as follows.

In the figure, four crystal directions are marked. For this cubic lattice, the band perpendicular to the crystal direction of [010] is that of the (020) lattice planes, the band perpen-
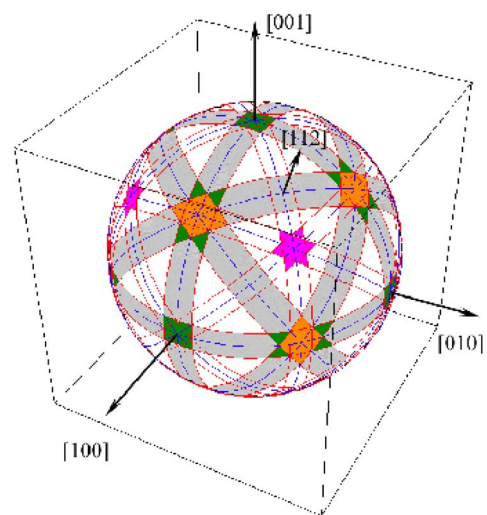

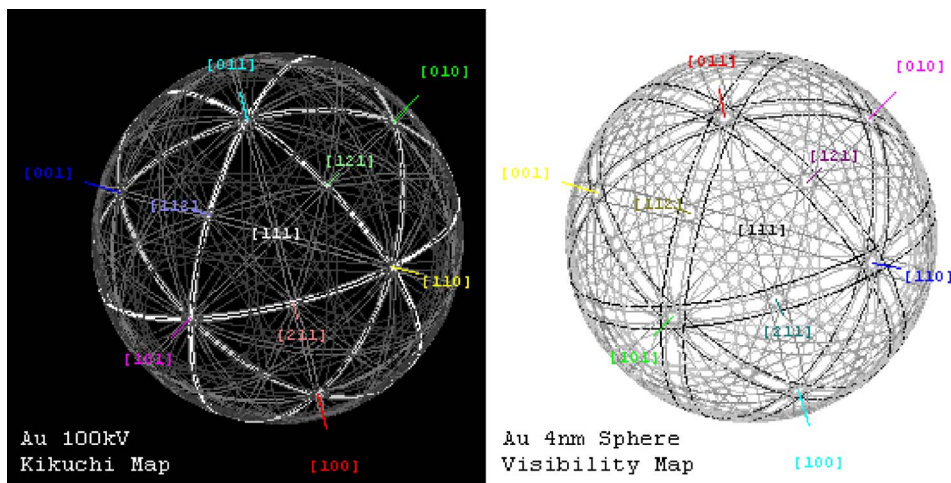FIG. 2. (Color online) One fringe-visibility map for a spherical fcc crystal.

FIG. 3. (Color online) Comparison of a Kikuchi map (left) to a fringe-visibility map (right) for a $t=4$ nm single-crystal gold sphere imaged at 100 kV. To first order, bandwidths in the former (where $t \gg t_{crit}$) are proportional to λ/d, while bandwidths in the latter (where $t \ll t_{crit}$ are proportional to d/t. Band boldness and d spacing are correlated.

dicular to [001] is the band of the (002) lattice planes, etc. The map contains bands of {111}, {002}, and {220} lattice planes, with those of the first two classes of lattice-plane sets drawn as shaded. The absence of other bands in Fig. 2 suggests that the smallest lattice spacing reliably imaged by the TEM in this model is d_{220}.

C. Applications

As shown in Fig. 3, Kikuchi maps depend primarily on electron wavelength while fringe-visibility maps are affected primarily by specimen thickness. Applications of Kikuchi maps to reciprocal-space exploration are well known. Widespread availability of crystallographic information in direct-space images is young, and applications for fringe-visibility maps are only beginning to emerge. We discuss a few here, namely, determination of lattice parameters, local measurement of specimen thickness, and "fringe" or "cross-fringe" fingerprinting of randomly oriented particle collections. Interactive maps useful for these tasks are easy to construct, for example, using the MATHEMATICA-based LIVEGRAPHICS3D applet by Kraus for implementation on the web.

1. Single-particle lattice parameters

An efficient way to determine lattice parameters is by the acquisition of three lattice covectors whose linear combinations span the entire reciprocal lattice,[11] Two of the three covectors may be inferred from a single zone-axis image. For example,[31] a fcc WC_{1-x} ($a=4.248$ Å) nanocrystal was examined with a Gatan double-tilt holder ($\pm15°$ around the side-entry goniometer tilt axis and $\pm10°$ around the second tilt axis). The fringe-visibility map (reliably seen fringes) involved only the shaded {111} and {002} bands in Fig. 2. Lattice parameters were determined directly from (200), (020), and (11$\bar{1}$) fringes seen down the [001] and [112] zone-axis directions.

This acquisition protocol required a total tilt range of 35.3°. The maximum tilt achievable with the double-tilt holder is 35.6°, barely higher than the tilt required. Because of this limitation only particles at one goniometer extreme, with the correct azimuthal orientation, were candidates for the experiment. Specifically, the [001] zone-axis image was

identified from a crystal, among thousands, at the holder setting of (15°, 9.7°). This crystal's [001] zone was azimuthally oriented so that the [112] zone axis was obtained after tilting to (−15°, −9.7°).

Thus only a small subset of particles using one specific protocol was eligible for this measurement. Improvements in microscope resolution and goniometer range are in the works. Recent progress in resolution enhancement by aberration correction opens up myriad opportunities for image-based crystallography.[39–41] The number of protocols increases at least quadratically with the microscope point resolution.[42] Accordingly, the fringe-visibility band map will contain more bands and band intersections. Figures 4(a) and 4(b) show fractions of visibility band maps for an 80 Å Al crystal at point resolutions of 1 and 0.6 Å, respectively. It is clear that an improvement of continuous contrast transfer results in an increase of the number of visibility bands encountered. Thus the choice of protocols to use for lattice-parameter determination will multiply, even were the available tilt range to remain fixed. The modified optics of aberration-corrected microscopes will also allow room for a wider range of specimen tilts.

The increase in possible analysis strategies might therefore overwhelm one's hope to "make sense of all those fringes" found on tilting of a randomly oriented unknown crystal encountered during microscope investigation. As shown in Fig. 4(c), this is especially problematic if the specimen is very thin. We therefore propose a protocol based on the properties of "a fringe-visibility map revealed piecemeal," as one begins to examine fringes seen in the candidate unknown under initially small exploratory tilts.

The approach is based on the one developed for identification of 100 nm mineral crystallites in an unequilibrated mix by selected area diffraction.[43] It may be broken down into the following steps.

(1) Begin with a crystal orientation at which the nanocrystal shows a set of fringes. If no fringes are visible, then the crystal is to be tilted randomly until fringes appear. For example, imagine beginning at the point marked "start" in the fringe-visibility band map shown in Fig. 5.

(2) Tilt the crystal around an axis parallel to the fringes, until the center of the visibility band is located.
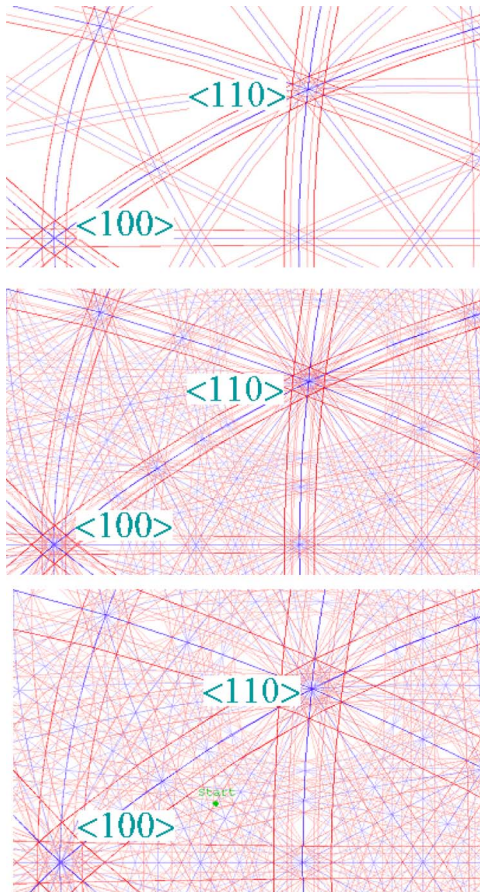
FIG. 4. (Color online) Visibility band map sections for an 80 Å Al crystal at point resolutions of (a) 1 (b) 0.6, and for a (c) 30 Å Al crystal at a point resolution of 0.6 Å. Improvement in the point resolution results in an increase of the number of resolvable lattice planes, and hence that of visibility bands [from (a) to (b)]. Reduction of the crystal size enables us to visualize lattice planes over a wider range angles, so that the width of the bands gets larger [from (b) to (c)].

(3) Tilt the crystal around an axis perpendicular to the fringes, until a cross-fringe intersection (labeled "Zone A" in the map) with another band is encountered.

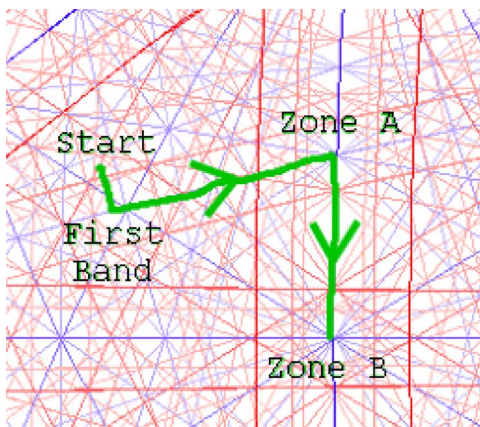(4) Similarly tilt the crystal around an axis parallel to the

FIG. 5. (Color online) Visibility band map section at 0.6 Å resolution, showing a trajectory for acquiring three basis-fringe (reciprocal lattice) vectors from a randomly oriented unknown. Minimizing beam-direction errors in the measured lattice parameters mandates that as wide a range of tilts as possible be used in the determination.

second band, until the center of zone A is located. Record lattice spacings and goniometer settings.

(5) Tilt the crystal around an axis perpendicular to the second band, until a second cross-fringe intersection (labeled "Zone B" in the map) with the third band is encountered.

(6) Repeat the work described in (4) for the third band, to position the beam at the center of that zone and record its positions and lattice spacings as well. Calculate an oriented basis triplet, i.e., scope coordinates of a randomly chosen lattice basis.[11]

(7) Repeat (5) and (6) to include zones at increasingly larger tilt angles as needed to improve the accuracy of the oriented-basis-triplet determination.

The basis triplet may at this point be reduced to a conventional form, assuming that measurement errors are small enough. The precision of lattice-parameter determination can be improved incrementally by the measurement of more lattice fringes over a wider range of tilts. Best-fit parameters are easily updated in least-squares fashion as a new set of fringes appears, and each fringe beyond the first three allows one to estimate the precision in each direction quantitatively. For example, diffraction studies indicate that lattice-parameter uncertainties in the untilted beam direction are the largest, and are most dependent on the incorporation of spacings observed over a range of tilts.[11]

This protocol depends on one's ability to tilt precisely by small angles in user-chosen directions. Modern double-axis goniometers can do this using computer support, with two caveats: (i) mechanical hysteresis leaves one with a mismatch between goniometer reading and the actual tilt, and (ii) the specimen will move laterally on the nanometer scale. The microscopist can generally solve the second problem by translating to keep the nanocrystal of interest in the field of view. The problem of tilt hysteresis is more fundamental, and will likely have to be addressed by independent feedback to verify stage orientation at a given instant. Quantitative metrology with scanning probe microscopes requires independent verification of the probe's lateral position, instead of orientation, but the technologies used there (e.g., optical or capacitive feedback sensing) may be relevant in both cases.

2. Random particle fringe fingerprints

For a randomly oriented nanocrystal, the probability that a set of lattice fringes will be visible is simply proportional to the solid angle subtended by the corresponding fringe-visibility band. For example, with the randomly oriented spherical fcc nanocrystal whose visibility band map is shown in Fig. 2, the probability of seeing (020) lattice planes is equal to the fraction of the 4π solid angle subtended by the (020) visibility band. Thus the probability of seeing a given fringe is simply the whole-band solid angle divided by 4π, or $p_{hkl} = \sin[\alpha_{hkl}]$ where α_{hkl} is α_{max} for $\{hkl\}$ fringes.

The probability of seeing *a pair of cross fringes* is proportional to the solid angle subtended by the corresponding visibility-band intersections, and hence, e.g., for [001] zone-axis fringes to the area of the [001] square in Fig. 2. As shown in Appendix C, the solid angle subtended by a square

TABLE I. Zone\band counts and probabilities for fcc crystals with a =4 Å and t=50 Å.

Zones\bands	g_{111}	g_{200}	p_{uvw}/zone	No. of zones
$\langle 110 \rangle$	2	1	0.003	6
$\langle 100 \rangle$	0	2	0.001	3
p_{hkl}/band	0.046	0.040		
No. of bands	4	3		

intersection of bands [from Eq. (C3)] is approximately $(2\alpha_{max})^2$. Hence the probability of seeing the associated cross-fringe pair is $p_x \cong 2\alpha_{max}^2 / \pi$. More generally, for an intersection between a band of half-width α_1 and another of half-width α_2 at an angle of ϕ, the cross-fringe probability is

$$p_x \cong \frac{2\alpha_1 \alpha_2}{\pi \sin[\phi]}. \qquad (2)$$

Using a visibility factor of $\Gamma=0.8$ estimated from Au/Pd nanoparticles evaporated on a thin carbon film, p_x for the [100] zone in a WC_{1-x} specimen was predicted to be about 1/700, consistent with experimental observation.[31] Estimation of such fringe probabilities in turn can be used to quantitatively fingerprint collections of randomly oriented nanoparticles, according to the fringes and interspot angles in lattice images.[44]

One can begin this process with a probability table for the visible fringes expected from a given type of crystal. For example, Table I lists the probabilities expected for the two largest lattice periodicities in a collection of 50 Å fcc particles with a lattice parameter of 4 Å. Here p_{uvw} is the probability of encountering a fringe pair for the [uvw] zone. From a table like this, for the system of interest, one can construct a template like that in Fig. 6 for plotting cross-fringe and fringe-histogram[45] data.

Figure 6 is designed to plot cross-fringe data points (two per spacing pair) and spacing histograms measured manually from multiparticle lattice-fringe images. However, it is also patterned after the layout of a fringe angular covariance map.[44] Fluctuation microscopy,[46] used, e.g., to characterize medium-range order in paracrystalline specimens,[47] historically has focused on the spacing-only or "powder" component of the pair-pair information available in a combined spatial and angular correlation analysis of image data from complex materials. The layout of Fig. 6, which looks at "patches of correlated periodicity as a function of angular lag" in a given size range, also preserves information on the angle between periodicities for such fluctuation analyses. Such plots may therefore prove useful in the automated analysis of high-resolution transmission electron microscopy (HRTEM) images as well.

Probability expressions flowing from fringe-visibility maps also allow one to quantify the relative abundance of particles with only one visible fringe set, versus those with cross fringes. For example, it nicely explains the fact that 2 nm particles with cross-fringes are often more abundant than those with single fringes. This is illustrated in Fig. 7, which plots the fraction of particles with $\langle 110 \rangle$-zone cross
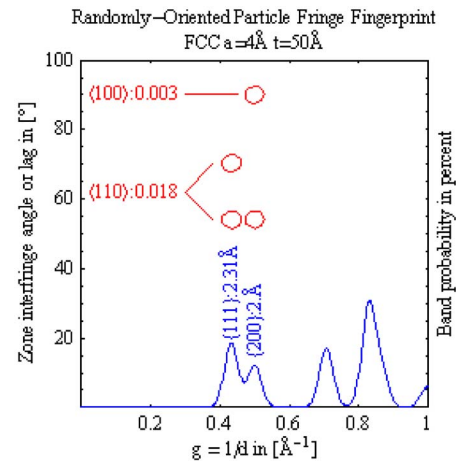

FIG. 6. (Color online) Template for fringe-visibility fingerprinting of randomly oriented fcc nanoparticle collections. Histogram peak heights equal single-fringe probabilities. Gaussian peak widths are schematically set at Γ/t to mimic the lateral broadening of reciprocal lattice spots, even though finite thickness under variable tilt actually creates high-frequency tails, i.e., spacing underestimates (Ref. 49). Circles mark where randomly oriented nanoparticle cross fringes are expected, with the labeled probabilities.

fringes, versus the fraction with only a single {111} fringe. Our observations suggest that the size at which this crossover occurs is quite sensitive to viewing conditions, and thus to visibility factor Γ.

The precision of fringe measurements in such images[48] is limited by shape anisotropy[49] and other tilt distortions.[50–53] Nonetheless the foregoing analysis works in practice, at least to first order, and provides a framework for a more careful study of these deviations as well.

3. Small-tilt thickness estimates

The reduction of crystal size is well known to result in reciprocal-space broadening of diffraction intensities as seen in x-ray, electron, and neutron diffractions. A formula, derived by Scherrer for a thesis on colloids around 1915, correlates such a broadening with the inverse of the mass-weighted average grain size.[54,55] More generally, the integral breadth of a diffraction spot, for small Bragg angles, is the reciprocal of the volume-averaged crystal dimension in the
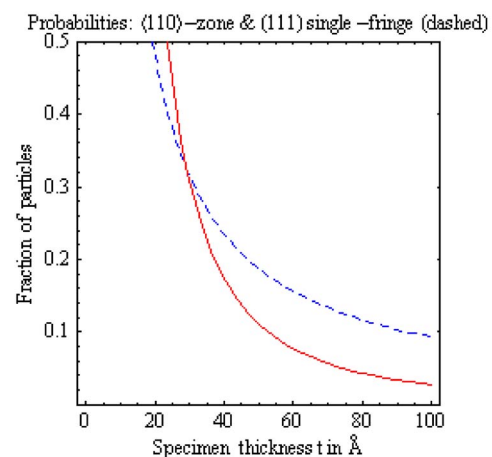

FIG. 7. (Color online) The crossover in abundance of cross-fringe vs single-fringe particles, with decreasing size.
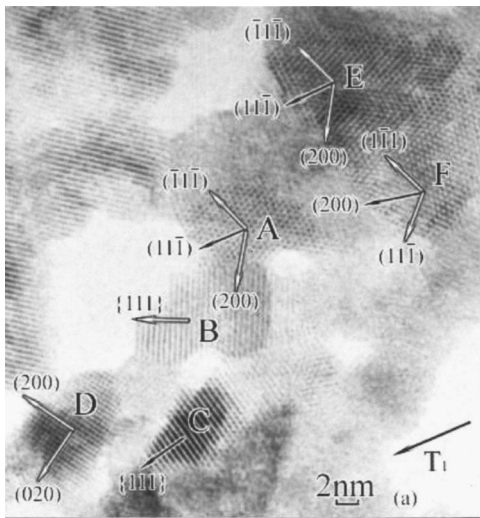
FIG. 8. HRTEM images of six WC_{1-x} nanocrystals showing lattice fringes that become invisible or remain visible after a single tilt of 14.5° around the side-entry goniometer tilt axis. The projection direction of the side-entry goniometer tilt axis T_1 is labeled at the bottom right corner.

FIG. 9. HRTEM images of the six WC_{1-x} nanocrystals in Fig. 8, after a single tilt of 14.5° around the side-entry goniometer tilt axis.

direction of that reflection.[56] As shown above, decreasing size causes visibility-band broadening as well. Here, we discuss how band broadening can help investigate local specimen thickness.

Given a crystal's size, lattice, and its orientation with respect to the tilt axis, the tilt sensitivity of lattice fringe visibility can be predicted. This is done by determining when the intersection between the reciprocal lattice spot and Ewald sphere decreases below an intensity threshold for fringe detectability with tilt, given the angle between the fringes and the tilt direction.[57,58] In order for the reciprocal lattice spot's intersection with the Ewald sphere to retain the intensity needed for fringe detection, the angular deviation of the reciprocal lattice vector from the tilt axis (or equivalently between fringe lines and the tilt direction) must be less than an upper limit ϕ that (following Appendix D) obeys

$$\sin\left[\frac{\theta_{range}}{2}\right] = \frac{\sin \alpha_{max}}{\sin \phi}. \tag{3}$$

Here α_{max} is given by Eq. (1). If ϕ is the angle between an observed fringe and the tilt direction, then θ_{range} is the tilt range over which that fringe is visible. Alternatively, if θ_{range} is an experimentally applied tilt, then fringes whose angle to the tilt direction is more than ϕ will become invisible because of the lowered intensity of the reciprocal lattice spot intersection with the Ewald sphere after tilt. In this latter application, we will refer to ϕ in Eq. (3) as ϕ_{max}.

Equations (1) and (3) have been used to predict lattice-fringe visibility after tilt for WC_{1-x} nanocrystals, as shown in Fig. 8. In the figure, each lattice-plane set has been labeled with both the Miller indices and an arrow representing the lattice-fringe normal. The length of the arrow is proportional to $1/d$. Hollow arrows are used for lattice fringes that are predicted to become necessarily invisible, and solid arrows for those with certain probabilities to do so, after tilt, as shown in Fig. 9. Take those three sets of lattice fringes of crystal A shown in Fig. 8, which are those of the WC_{1-x}
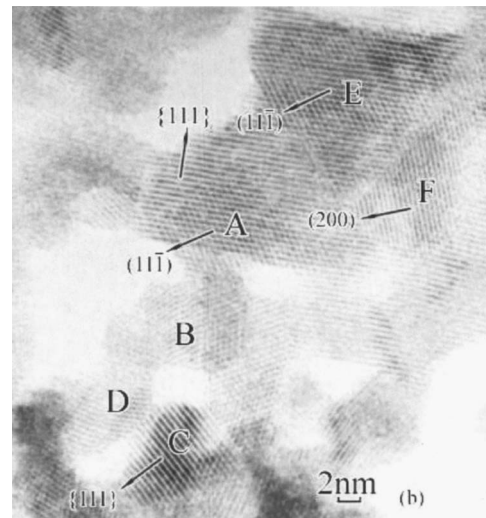
$(-1,1,-1)$, $(1,1,-1)$, and $(2,0,0)$ lattice planes, as examples. The average projection size of crystal A is about 48 Å. Equation (3) predicts that for the given amount of tilt,

$$\phi(\Gamma = 0.79, t = 48 \text{ Å}, d_{111} = 2.453 \text{ Å}) = 20.6°, \tag{4}$$

and

$$\phi(\Gamma = 0.79, t = 48 \text{ Å}, d_{002} = 2.124 \text{ Å}) = 18.3°. \tag{5}$$

The three lattice-fringe normals deviate from the projection of T_1 by 69.1°, 0.3°, and 56.6°, respectively. Among them the first and the third are larger than their corresponding limits obtained in Eqs. (4) and (5). Therefore, the $(-1,1,-1)$ and $(2,0,0)$ lattice fringes are predicted to become invisible after tilt. This is shown to be true in Fig. 9. This way the invisibility of 9 out of 13 lattice-fringe sets is predicted, which is consistent with the HRTEM observation. The results are shown in Table II.

In Fig. 8, the nine lattice-fringe sets which are predicted to become invisible after tilt are labeled with hollow arrows.

TABLE II. Correlating Eq. (3) in predicting lattice-fringe invisibility after tilt with HRTEM observation, as shown in Figs. 8 and 9. Quantities in the third and fifth columns are obtained from Fig. 8 before tilt, and column 7 contains a theoretical prediction of invisibility after tilt for comparison to the experimental result from Fig. 9 in column 8.

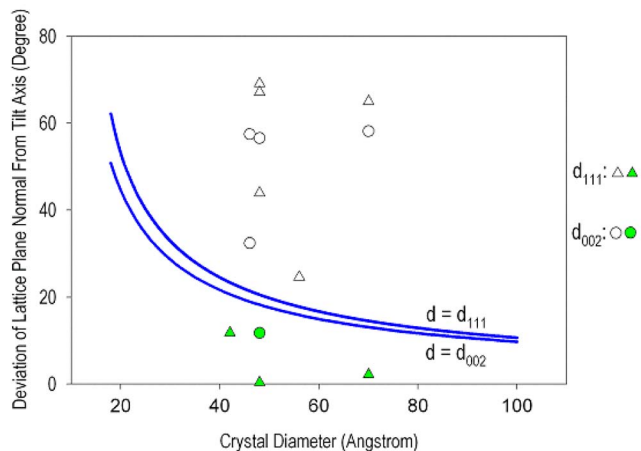| ID	$\theta°$	$t(\text{Å})$	(hkl)	$\phi°$	$\phi°_{max}$	$\phi/\phi_{max} > 1$?	Invisible?
A	14.5	48	$(1,1,-1)$	0.3	20.6	No	No
			$(-1,1,-1)$	69.1		Yes	Yes
			$(2,0,0)$	56.6	18.3	Yes	Yes
B		56	$(1,1,1)$	24.6	17.8	Yes	Yes
C		42	$(1,1,1)$	11.8	23.4	No	No
D		46	$(2,0,0)$	57.5	19.0	Yes	Yes
			$(0,2,0)$	32.5		Yes	Yes
E		70	$(1,1,-1)$	2.2	14.5	No	No
			$(-1,1,-1)$	65.0		Yes	Yes
			$(2,0,0)$	58.2	13.1	Yes	Yes
F		48	$(1,-1,1)$	67.1	20.6	Yes	Yes
			$(1,1,-1)$	43.9		Yes	Yes
			$(2,0,0)$	11.8	18.3	No	No

FIG. 10. (Color online) A plot of the maximum angular deviation of a reciprocal lattice vector from the tilt axis, as given by Eq. (3), over the crystal size. Above such a limit the reciprocal lattice spot necessarily loses intersection with the Ewald sphere after tilting the crystal by 14.5°. Experimental data from Fig. 8 and 9 are also shown, with hollow symbols used for the lattic-fringe sets observed to become invisible after tilt.

Please note that all these lattice-fringe sets disappear in Fig. 9, which is an indication of the consistency of the model with the HRTEM observations.

Figure 10 shows the plots of ϕ_{max} versus thickness with $\theta_{range} = 14.5°$ and $\Gamma = 0.79$ for $d_{111} = 2.453$ Å and $d_{002} = 2.124$ Å. Also shown in figure are the experimental data from Fig. 8. Hollow symbols are used to label lattice-fringe sets that are observed to become invisible after tilt, as shown in Fig. 9, and solid symbols for the rest. A consistency between the model and experimental observation is indicated, since all the hollow symbols are above their corresponding curves.

As proof of the concept in hand, one can easily solve Eqs. (1) and (3) for specimen thickness t. Considering only the dominant term, for example, one gets

$$t \cong \Gamma d \csc\left[\frac{\theta_{range}}{2}\right] \csc[\phi], \qquad (6)$$

where ϕ (as above) is the projected angle between the lattice fringe and the tilt direction. Plots of t/Γ vs θ_{range} for various ϕ allow one to plot measured ϕ and θ_{range} values, and to see how their uncertainties affect the inferred t/Γ.

The expression above suggests a fractional error in thickness, per unit error in tilt range, of $(1/t)\delta t / \delta\theta \sim t \sin[\phi]/(\Gamma d)$. For example, this predicts a 15% error in the thickness, per degree of error in tilt range, for a 50-Å-thick foil with a 2 Å fringe 20° from the direction of the tilt. This measurement of specimen thickness requires only verification by the microscope operator that the tilt range over which the fringe remains visible is about 13°. High precision goniometers, e.g., with a verifiable tilt, and a way to profile fringe visibility for small increments in tilt, could thus make it possible to routinely measure nanocrystal thickness at many points in an image with only minor amounts of tilt. With such instrumentation, experimental profiles of fringe intensity as a function of tilt like those modeled in Appendix E could open up a world of real-time quantitative analysis.
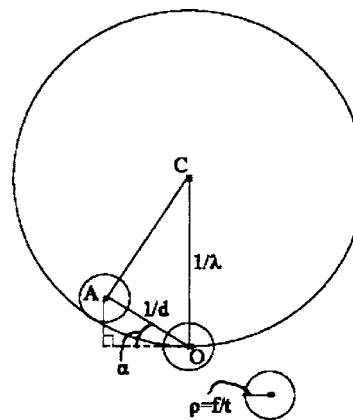

FIG. 11. Ewald sphere geometry for equant-particle fringe visibility. Here **C** is the sphere's center, **O** is the origin of the reciprocal lattice, and **A** is the center of a reciprocal lattice spot.

IV. CONCLUSIONS

Fringe visibility versus orientation for a set of lattice planes, relative to the incident electron beam, in specimens of given thickness is well represented by a "visibility band." The bands of all lattice planes reliably detected within the point resolution of a microscope, during a given exposure, make up a fringe-visibility map. Like Kikuch maps in reciprocal space, fringe-visibility maps serve as roadmaps for exploring orientation in direct space. We illustrate how they can be useful in determining the 3D lattice parameters of an arbitrary nanocrystal, for fingerprinting fringe and cross-fringe abundances in a collection of randomly oriented nanocrystals, and for determining the local thickness of crystalline specimens with modest amounts of tilt given a sufficiently precise goniometer. Fringe-visibility maps and these applications will be even more useful in aberration-corrected microscopes capable of subangstrom resolution, provided attention is given (during their design) to the precise control and *verification* of specimen orientation.

APPENDIX A: THE VISIBILITY-BAND OUTER HALF-ANGLE

Figure 11 illustrates the geometry of a simple model for fringe visibility from an equant (i.e., spherical) particle. Visibility requires that the reciprocal lattice "spot" intersect the Ewald sphere. Point **O** is the origin of the reciprocal lattice, and two reciprocal lattice spots are shown a distance $1/d$ away from the center. Since the effective radius of the reciprocal lattice spots is affected by many factors, it is written as Γ/t, where t is the thickness of the crystal and Γ is a visibility factor. This visibility factor will be a number on the order of 1 that depends on the method of periodicity detection, the range of angles in the illuminating beam, the microscope's response function, and the amount of "fringe obscuring" noise in the field of the image. It may need to be determined

experimentally. As a specimen is tilted, the reciprocal lattice spots will come in and out of contact with the Ewald sphere. In Fig. 11, the outermost edge of the reciprocal lattice spot is tangent with the Ewald sphere defining a critical angle, α, at which fringes of the corresponding spacing would be viewable in a direct-space image. We derive α as follows.

Since the radius of the Ewald sphere is $1/\lambda$, where λ is the electron wavelength, we can define the length from the center of the Ewald sphere **C** to the center of the reciprocal lattice spot **A** as $1/\lambda - \Gamma/t$. The distance from the center of the Ewald sphere to the center of the reciprocal lattice will be $1/\lambda$ and the spacing between the reciprocal lattice spots will be $1/d$. If α is the angle defining the maximum tilt of the reciprocal spot before loss of fringe visibility, then we can use plane trigonometry's law of cosines for the complement of angle α in triangle **CAO**, namely,

$$\left(\frac{1}{\lambda} - \frac{\Gamma}{t}\right)^2 = \frac{1}{d^2} + \frac{1}{\lambda^2} - \frac{2}{d\lambda}\cos\left[\frac{\pi}{2} - \alpha\right], \quad (A1)$$

to obtain

$$\sin[\alpha_{max}] = d\frac{\Gamma}{t} + \frac{\lambda}{2d}\left[1 - \left(d\frac{\Gamma}{t}\right)^2\right]. \quad (A2)$$

The first term (due to beam-direction broadening of the reciprocal lattice spot) dominates in HRTEM of nanocrystals because d/t is typically greater than λ/d. The equation may also be relevant to electron channeling, electron-backscatter diffraction, and (with an added factor of 1/2) Kikuchi bands. However, in these cases the λ/d term typically dominates, yielding a $1/d$ rather than d dependence for small-angle bandwidths.

APPENDIX B: THE INNER HALF-ANGLE CRITICAL THICKNESS

If the specimen is sufficiently thick, or electron wavelengths sufficiently large, images taken with a parallel beam might also show loss of fringe visibility when the specimen is oriented on the zone axis, i.e., between Bragg conditions for diffraction from either side of a set of lattice planes. This condition would introduce an "invisibility stripe" down the center of the visibility band depicted in Fig. 1.

Although the large Bragg angles and thick specimens used for x-ray diffraction make this a common occurrence, it is rare in electron lattice imaging because of the thin nature of the specimens and the small electron wavelength. To confirm this, consider the drawing in Fig. 12. Note that the length of segment **AC** is $1/\lambda + \Gamma/t$, the length of segment **BC** is $1/d$, and the length of segment **AB** is $1/\lambda$. Hence from Pythagoras' theorem for right triangle **ABC**, t becomes

$$t_{crit} = \frac{\Gamma d}{\sqrt{1 + (d+\lambda)^2 - d/\lambda}}. \quad (B1)$$

Putting in typical numbers for these quantities shows that this condition is seldom met for specimens thin enough for electron phase-contrast imaging, particularly if the effects of beam broadening (i.e., a range of angles in the incident beam) are taken into account. For thicknesses great enough,
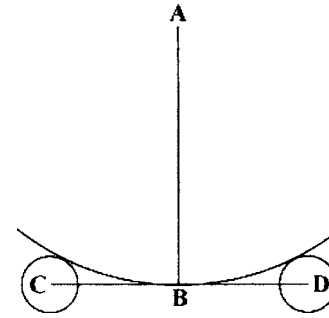

FIG. 12. Schematic configuration with an electron beam travelling down a zone axis, and with reciprocal lattice spots are tangent to the Ewald sphere from the outside. The arc centered at **A** represents part of the Ewald sphere. Segments **BC** and **BD** represent the reciprocal lattice vectors, i.e., $BC = g$ and $BD = -g$. The circles centered at **C** and **D** represent the reciprocal lattice spots. It is obvious that **CD** is perpendicular to **AB**.

simply changing the sign of Γ/t in Eq. (A2) tells us that the half-width α_{min} of the invisibility stripe will obey

$$\sin[\alpha_{min}] = \frac{\lambda}{2d}\left[1 - \left(d\frac{\Gamma}{t}\right)^2\right] - d\frac{\Gamma}{t}, \quad (B2)$$

where the first term is the dominant one.

APPENDIX C: ESTIMATING BAND INTERSECTION AREAS

Consider first the case of equal bands intersecting at right angles, as shown in Fig. 13. We are interested in σ_2, twice the area σ_1 of one intersection, because great-circle bands intersect twice on the opposing sides of the orientation unit sphere. For the inscribed circle shown in the figure, the "double-sided solid angle" is $4\pi(1 - \cos\alpha)$. The double-sided solid angle of the circumscribed circle is approximately $4\pi[1 - \cos(\sqrt{2}\alpha)]$.

For $\alpha < \pi/4$, the *exact* value of the intersection solid angle[59] is

$$\sigma_1 = 8\sum_{n=1}^{\infty} \frac{(-1)^{n+1}\sin[\alpha]^{2n}}{n!} F[n] \prod_{k=1}^{n}\left(\frac{3}{2} - k\right)$$

$$= 4\alpha^2 + \frac{2}{9}\alpha^6 + \frac{8}{45}\alpha^8 + \cdots, \quad (C1)$$

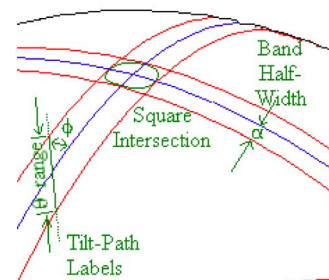where hypergeometric function $F[n]$ is

FIG. 13. (Color online) Visibility bands, a tilt path, and a "cross-fringe" intersection on the surface of a unit sphere.
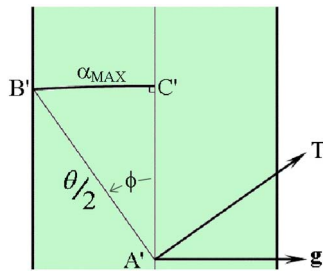
FIG. 14. (Color online) A segment of a continuous visibility band, with half of the visibility "tilt range" marked by segment $A'B'$.

$$F[n] \equiv \sum_{m=0}^{n-1} \frac{(n-1)!}{m!\,(n-1-m)!} \frac{1}{2m+1}. \tag{C2}$$

For $\alpha > \pi/4$, the upper and lower visibility zones connect leaving only four circular "cross-free caps." Hence σ_1 then becomes $2\pi(2\sin[\alpha]-1)$.

These observations show that an excellent approximation for small angles is $\sigma_2 \cong 2(2\alpha)^2$, i.e., twice the area one would calculate for a flat square of side 2α. The approximation error is to first order $(4/9)\alpha^6$, and is still below 0.5% when bandwidth 2α is a radian.

More generally, the bandwidth half-angles (e.g., α) follow from the elements described in Appendix A, namely, the lattice spacing, specimen thickness, and electron wavelength. When crossing bands have half-angles of α_1 and α_2, and intersect at an angle of ϕ radians, the flat polygon estimate becomes

$$\sigma_2 \cong \frac{2(2\alpha_1)(2\alpha_2)}{\sin[\phi]}. \tag{C3}$$

Given the value (or an estimate) for visibility-band intersection solid angles, the probability of seeing cross fringes in a randomly oriented particle is then (assuming negligible zone overlap) simply $p_x = n\sigma_2/(4\pi)$, where n is the zone multiplicity, e.g., $n=3$ for $\langle 100 \rangle$ zone cross fringes from a cubic crystal.

APPENDIX D: THE TILT RANGE FOR FRINGE VISIBILITY

The angular range over which a set of lattice planes remains visible is smallest if the tilt axis is parallel to the planes. Half of this angular range is then given by Eq. (1). Generally, the tilt axis is not parallel to the lattice planes. To take advantage of band symmetry, we begin with the electron beam initially parallel to the lattice planes, as shown in Fig. 14. The tilt range for fringe visibility is then easily quantified.

The figure displays a visibility band segment. $A'C'$ is the trace of the lattice plane, A' is the starting electron-beam direction, T is the tilt axis, and g is the reciprocal lattice vector. T and g make an angle of ϕ. Since $B'C' \perp A'C'$, $B'C' = \alpha_{max}$ is half of the visibility bandwidth. $A'B'$ is the tilt path of the electron-beam direction and is half the total tilt range θ within which the lattice fringes are visible (the other half is symmetric with $A'B'$ about A'). The following relationships are obvious from the figure: $A'B' \perp T, \angle B'A'C'$
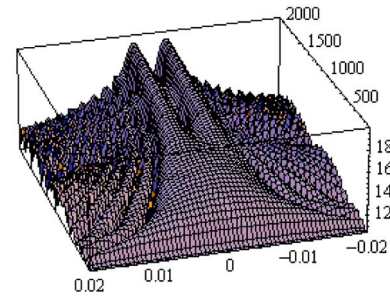

FIG. 15. (Color online) Logarithmic fringe-intensity profile ($d=2$ Å and $\lambda =0.01$ Å) for a spherical particle whose diameter t is given in angstroms by the top-labeled axis (running front to back), as a function of "tilt from edge-on in radians" on the bottom-labeled axis (running left to right).

$= \phi$, and each of $A'B'$, $B'C'$, and $C'A'$ is an arc of a great circle. Spherical trigonometry's law of sines then yields

$$\sin[\alpha_{max}] = \sin[\phi]\sin[\theta/2]. \tag{D1}$$

APPENDIX E: FRINGE-VISIBILITY ROCKING CURVES

Given the shape of a nanocrystal, the vector separation between a reciprocal lattice point and the Ewald sphere allows one to calculate the Fourier intensity of an individual fringe as a function of orientation. Replacing Γ/t with deviation parameter or excitation error s in Eq. (1) and solving give the magnitude of this vector separation

$$s = \left| \frac{\sqrt{1+(\lambda/d)^2 - 2(\lambda/d)\sin[\alpha]} - 1}{\lambda} \right|, \tag{E1}$$

where α is an arbitrary tilt of the beam direction from edge on.

Because fringe-intensity profiles concern not just the boundaries of fringe visibility, dynamical contrast effects must be taken into account, particularly for crystal thicknesses near to or larger than an extinction distance.[33,34] Here, however, we illustrate such profiles or rocking curves for the simplest case, namely, a spherical particle of diameter t in the kinematic approximation. For such a particle, the shape transform[60,61] as a function of spatial frequency g (again using signal-processing conventions) is simply

$$\Xi = \frac{\sin[\pi g t] - \pi g t \cos[\pi g t]}{2\pi^2 g^3}. \tag{E2}$$

Consider a lattice plane canted by α radians from the edge-on position along the electron-beam direction. Since all reciprocal lattice spots will be convolved with the shape transform, one can add amplitudes (in the coherent scattering case) from both sides of the lattice plane by adding Ξ values for deviation s evaluated at $\pm\alpha$. Figure 15 illustrates.

Note that for small thicknesses the fringe-intensity profile shows the expected (d/t) dependence of its angular half-width. For spheres with a diameter greater than 650 Å, the rocking curve bifurcates into the fixed (λ/d) band width cut by the reduced-visibility stripe predicted in Appendix B. This is therefore an alternate view of the transition between thick specimen electron-channeling/Kikuchi map (λ/d) and thin specimen fringe-visibility map (d/t) geometries. Bend con-

tours of suitably oriented wedge-shaped crystals thus (cf. Fig. 9 to Hashimoto *et al.*[62] and Graef[37]) bridge the gap experimentally between both extremes.

[1]H. Kung and T. Foecke, MRS Bull. **24**, 14 (1999).
[2]W. A. Jesser, G. Shiflet, G. Allen, and J. Crawford, Mater. Res. Innovations **2**, 211 (1999).
[3]M. Wautelet, Nanotechnology **3**, 42 (1992).
[4]M. Wautelet, Nanotechnology **12**, 68 (2001).
[5]W. M. Tolles, MRS Bull. **25**, 36 (2000).
[6]P. Fraundorf, Ultramicroscopy **22**, 225 (1987).
[7]R. Henderson and P. N. T. Unwin, Nature (London) **257**, 28 (1975).
[8]R. P. Goehner and P. Rao, Metallography **10**, 415 (1977).
[9]R. Bonnet, J. Microsc. Spectrosc. Electron. **3**, 77 (1978).
[10]K.-X. Guo, Acta Phys. Sin. **27**, 160 (1978).
[11]P. Fraundorf, Ultramicroscopy **6**, 227 (1981).
[12]P. Fraundorf, Ultramicroscopy **7**, 203 (1981).
[13]J. M. Cowley, J. Electron Microsc. **45**, 3 (1996).
[14]P. Tambuyser, J. Mater. Sci. Lett. **3**, 184 (1984).
[15]Q. Liu, Micron Microsc. Acta **20**, 261 (1989).
[16]Q. Liu, Q.-C. Meng, and B. Hong, Micron Microsc. Acta **20**, 255 (1989).
[17]Q. Liu, Micron Microsc. Acta **21**, 105 (1990).
[18]P. Möck, Cryst. Res. Technol. **26**, 653 (1991).
[19]P. Möck, Cryst. Res. Technol. **26**, 797 (1991).
[20]Q. Liu, X. Huang, and M. Yao, Ultramicroscopy **41**, 317 (1992).
[21]P. Moeck and W. Hoppe, *Tenth European Congress on Electron Microscopy* (Universidad de Grenada, Spain, 1992), Vol. 1, pp. 193–194.
[22]Z. S. Basinski, *Proceedings of the Fifth International Congress for Electron Microscopy* (Academic, New York, 1962), Vol. 1, p. B13.
[23]D. J. DeRosier and A. Klug, Nature (London) **217**, 130 (1968).
[24]J. M. Cowley, Ultramicroscopy **7**, 19 (1981).
[25]L. A. Amos, R. Henderson, and P. N. T. Unwin, Prog. Biophys. Mol. Biol. **39**, 183 (1982).
[26]A. V. Crewe and D. A. Crewe, Ultramicroscopy **16**, 33 (1985).
[27]J. Frank and M. Radermacher, in *Advanced Techniques in Biological Electron Microscopy*, edited by J. K. Koehler (Springer-Verlag, Berlin, 1986), Vol. II, pp. 1–72.
[28]H. R. Wenk, K. H. Downing, H. Meisheng, and M. A. O'Keefe, Acta Crystallogr., Sect. A: Found. Crystallogr. **48**, 700 (1992).
[29]J. Frank and M. Rademacher, Ultramicroscopy **46**, 241 (1992).
[30]J. R. Jinschek, H. A. Calderon, K. J. Batenburg, V. Radmilovic, and C. Kisielowski, Mater. Res. Soc. Symp. Proc. **839**, P4.5.1 (2005).
[31]W. Qin and P. Fraundorf, Ultramicroscopy **94**, 245 (2003).
[32]S. Nishikawa and S. Kikuchi, Nature (London) **121**, 1019 (1928).
[33]P. Hirsch, A. Howie, R. B. Nicholson, D. W. Pashley, and M. J. Whelan, *Electron Microscopy of Thin Crystals*, 2nd ed. (Robert E. Krieger, Huntington, New York, 1977).
[34]L. Reimer, *Transmission Electron Microscopy: Physics of Image Formation and Microanalysis*, 4th ed. (Springer, Berlin, 1997).
[35]D. C. Joy, in *Quantitative Scanning Electron Microscopy*, edited by D. B. Holt, M. D. Muir, L. M. Boswarva, and P. R. Grant (Academic, New York, 1974).
[36]J. A. Venables and C. J. Harland, Philos. Mag. **27**, 1193 (1973).
[37]M. D. Graef, *Introduction to Conventional Transmission Electron Microscopy* (Cambridge University Press, Cambridge, 2003).
[38]P. P. Ewald, Ann. Phys. **54**, 519 (1917).
[39]M. Haider, S. Uhlermann, E. Schwan, H. Rose, B. Kabius, and K. Urban, Nature (London) **392**, 768 (1998).
[40]P. Nellist and S. J. Pennycook, Phys. Rev. Lett. **81**, 4156 (1998).
[41]S. V. Aert, A. J. den Decker, and D. V. Dyck, Micron **35**, 425 (2004).
[42]P. Moeck, W. Qin, and P. Fraundorf, Mater. Res. Soc. Symp. Proc. **818**, Mll.3.1 (2004).
[43]P. Fraundorf, Geochim. Cosmochim. Acta **45**, 915 (1981).
[44]P. Fraundorf, E. Mandell, W. Qin, and K. Chop, in *Microscopy and Microanalysis* 10, Supplement 2 (Cambridge University Press, 2004), pp. 1262–1263.
[45]E. Mandell, P. Fraundorf, and M. F. Bertino, in *Microscopy and Microanalysis* 10, Supplement 2 (Cambridge University Press, 2004), pp. 1254–1255.
[46]P. M. Voyles, J. M. Gibson, and M. M. J. Treacy, J. Electron Microsc. **49**, 259 (2000).
[47]J. M. Gibson and M. M. J. Treacy, Phys. Rev. Lett. **78**, 1074 (1997).
[48]J. Biskupek, U. Kaiser, and A. Chuvilin, Microsc. Microanal. **9**, 166 (2003).
[49]B. E. Warren, Phys. Rev. **59**, 693 (1941).
[50]L. D. Marks, Ultramicroscopy **12**, 237 (1983).
[51]J. C. H. Spence, *Experimental High-Resolution Electron Microscopy*, 2nd ed. (Oxford University Press, Oxford, 1988).
[52]J.-O. Malm and M. A. O'Keefe, Ultramicroscopy **68**, 13 (1997).
[53]H. Kohno, N. Ozaki, H. Yoshida, K. Tanaka, and S. Takeda, Cryst. Res. Technol. **38**, 1082 (2003).
[54]P. Debye and P. Scherrer, Nachr. Ges. Wiss. Goettingen, Math.-Phys. Kl. **1916**, 1.
[55]A. L. Patterson, Phys. Rev. **56**, 978 (1939).
[56]B. E. Warren, *X-ray Diffraction* (Dover, New York, 1969).
[57]W. Qin, Ph.D. thesis, University of Missouri - St. Louis/Rolla, 2000.
[58]W. Qin and P. Fraundorf, in *Microscopy and Microanalysis* 6, Supplement 2 (Springer, New York, 2000), pp. 1040–1041.
[59]J. Bailey, UM-St. Louis Scanned Tip and Electron Image Lab Undergrad Student Project Report No. 10512, 2001 (unpublished).
[60]A. L. Patterson, Phys. Rev. **56**, 972 (1939).
[61]A. L. G. Rees and J. A. Spink, Acta Crystallogr. **3**, 316 (1950).
[62]H. Hashimoto, A. Howie, and M. J. Whelan, Proc. R. Soc. London, Ser. A **269**, 80 (1962).